Song et al. *NPG Asia Materials* (2025)17:12
https://doi.org/10.1038/s41427-025-00587-7

NPG Asia Materials

ARTICLE Open Access

Comprehensive modelling of ferrofluids via dual dissipation mechanisms for multiplexed thermal activation

Mingu Song[1], Dowoo Kim[1], Junte Heo[1], Daerl Park[1], Jaehyun Kim[1], Man Seung Heo[2] and Heon-Jin Choi[1]

Abstract

Ferrofluids, composed of magnetic nanoparticles (MNPs), act as magnetothermal energy transducers under alternating magnetic fields. Heat conversion occurs through two primary mechanisms: Néel relaxation and Brownian relaxation. However, establishing activation standards for each particle type remains challenging, with significant discrepancies between theoretical and experimental values. We propose that these discrepancies arise not only from the nonlinear responses of magnetic particles but also from the simultaneous occurrence of both heat generation mechanisms. To address this issue, we propose a refined equation that considers the dual dissipation of each relaxation process. This comprehensive model predicts the transduced power more accurately and helps trace the stochastic Brownian rotation inside magnetic colloidal suspensions. Furthermore, our approach theoretically proves the multiplexed activation with three (or more) channels, which cannot be verified using the conventional theory. This study offers insights into the selection of stable operations for magnetothermal energy conversion, whether in single or multiple channels.

Introduction

Ferrofluids (FFs), primarily composed of magnetic nanoparticles (MNPs), offer several advantages, including wireless operation for energy transduction, such as magnetothermal[1–3], magnetoelectric[4], and magnetomechanical[5,6]. Owing to the high transmittance of magnetic fields through non-magnetic materials[7], this non-invasive technology has been applied in biomedical applications, such as magnetic particle imaging[8,9] (MPI), cancer therapy[10,11](commonly referred to as magnetic hyperthermia), and agents for targeted drug delivery[12,13]. More recently, precise injection of minimal amounts of FFs has facilitated chronic deep brain stimulation[14], and multiplexed stimulations have subsequently been explored[15], laying the groundwork for state-of-the-art wireless neuromodulation. Additionally, non-invasive methods for traversing the blood-brain barrier (BBB) by magnetic force have been studied[16,17], potentially advancing the understanding of the correlation between brain areas and cognitive functions[18] of organisms, which remain mostly shrouded in mystery.

To effectively utilise and advance these applications, a meticulous design of MNPs is crucial, with careful consideration of the thermal energy generated. For instance, in brain stimulation, temperatures or rising rates are necessary to activate thermoreactive transient receptor potential (TRP) channels, such as TRPV1/TRPA1, in neuronal cells[1,19–21]. Similarly, temperatures above 43 °C are essential for inducing axonal nerve growth via Ca^{2+} influx[22]. Therefore, the accurate prediction and management of the heat generated by MNPs under an external magnetic field are critical for both therapeutic and remote outcomes, minimising risks[23] and increasing benefits.

Therefore, a solid theoretical framework is essential for enhancing the engineering applications of FFs in the biomedical field. The power dissipation of the FFs originates from two primary mechanisms: internal energy loss owing to the consistent reversal of the magnetic moment (Néel relaxation) and frictional loss of rotational motion

Correspondence: Heon-Jin Choi (hjc@yonsei.ac.kr)
[1]Department of Materials Science and Engineering, Yonsei University, Yonsei, Republic of Korea
[2]Advanced Institutes of Convergence Technology (AICT), Seoul National University, Seoul, Republic of Korea

© The Author(s) 2025
Open Access This article is licensed under a Creative Commons Attribution 4.0 International License, which permits use, sharing, adaptation, distribution and reproduction in any medium or format, as long as you give appropriate credit to the original author(s) and the source, provide a link to the Creative Commons licence, and indicate if changes were made. The images or other third party material in this article are included in the article's Creative Commons licence, unless indicated otherwise in a credit line to the material. If material is not included in the article's Creative Commons licence and your intended use is not permitted by statutory regulation or exceeds the permitted use, you will need to obtain permission directly from the copyright holder. To view a copy of this licence, visit http://creativecommons.org/licenses/by/4.0/.

(Brownian relaxation). To date, the Stoner-Wohlfarth model-based theories (SWMBTs) for major loop cycles and the first-order Debye model based on the linear response theory (LRT) for minor loop cycles have been used to quantify the amount of converted heat[24]. We began with the LRT model to develop an integrated theory despite the nonlinearity restriction between the field and magnetisation in MNPs. In a sufficiently low field, the relaxation of the MNPs is expressed in terms of the complex susceptibility:

$$\chi_{FF} = \frac{\chi_0}{1 + i\omega\tau_{eff}} \tag{1}$$

where ${\tau_{eff}}^{-1} = {\tau_B}^{-1} + {\tau_N}^{-1}$. This equation was first used by Debye[25] to describe the dielectric response, and Shliomis and Stepanov[26] derived the dynamic susceptibility of FFs. Rosensweig deduced an equation for power dissipation using the first law of thermodynamics[27]:

$$P_{FF} = \mu_0 \pi H_0^2 f \chi'' = \mu_0 \pi H_0^2 f \chi_0 \frac{\omega\tau_{eff}}{1 + (\omega\tau_{eff})^2} \tag{2}$$

This classical model describes the energy from the cyclic increase in internal energy due to the periodic magnetic potential and is particularly useful in mild conditions below the LRT limit ($H/H_K \leq 0.4$)[28] and biomedical safety limits[29] ($H{\cdot}f < 10^{10}$ Hz·A/m). However, in many studies, Eq. 2 failed to predict the experimental values accurately[30], highlighting the necessity of refining the conventional theory[31,32]. Here, we identified that the effective relaxation approach introduces inherent errors, assuming that the frictional loss per unit volume due to Brownian rotation and the hysteresis loss from Néel relaxation[24] are equal.

Néel relaxation is the process of transferring energy from the spin system to the lattice through spin-orbit coupling, which is converted into forms such as spin waves, lattice vibrations, and strains of MNPs[33]. On the other hand, Brownian relaxation involves purely rotational alignment, with frictional heat generated through effective collision with solvent molecules at the hydrodynamic surface of the MNPs. Consequently, although Eq. 2 remains logically valid (aside from the problems of LRT) for FFs containing static Néel-relaxing MNPs, the acceptance of Brownian rotation leads to an increase in the internal energy leaked through the rotation, resulting in a mathematical underestimation of the dissipated power, even if it matches the experimental data[34]. In other words, when the spin-reversal energy is larger than the energy for rotation, the magnetic moment aligns externally owing to the rotational motion of the MNPs, thereby reducing the potential heat generated from internal energy dissipation. This effect can be summarised using Eq. 3:

$$P_{FF} = (\mu_0 \pi H_0^2 f \chi'' - P_l) + P_r \tag{3}$$

where P_l represents the leakage of the cyclic increase caused by the rotational alignment of the MNPs, and P_r denotes the frictional heat generated by rotational motion. To calculate each term mathematically, it is imperative to initially distinguish between the combined susceptibilities. Hence, the magnetic susceptibility of the FFs can be expressed as the sum of Brownian and Néel susceptibilities, denoted as χ_B and χ_N, respectively[35].

$$\chi_{FF} = \chi_N + \chi_B = (\chi'_N + \chi'_B) - i(\chi''_N + \chi''_B) \tag{4}$$

$$\chi_N = \frac{\chi_{N0}}{1 + i\omega\tau_N}, \chi_B = \frac{\chi_{B0}}{1 + i\omega\tau_B} \tag{5}$$

where $\chi_B = f_B{\cdot}\chi_0$ and $\chi_N = f_N{\cdot}\chi_0$ are the initial susceptibilities of each relaxation mechanism, and f_B and f_N are the relaxation ratios ($f_B + f_N = 1$), which were calculated using the decay rates relative to each relaxation time: $f_B = {\tau_B}^{-1}/{\tau_{eff}}^{-1}$ and $f_N = {\tau_N}^{-1}/{\tau_{eff}}^{-1}$. This mathematical separation provides insights into the overall behaviour of the fluid, as shown in Fig. 1.

Figure 1a shows the separated complex susceptibilities, which were indistinguishable using previous methods (Eq. 1). Comparing this separation approach with existing theories, we observe that while the values of the real susceptibilities are consistent, there are noticeable deviations in the peak positions of the imaginary susceptibility for each mechanism. This discrepancy indicates the impact of amplitude-dependent relaxation models on the frequency of heat emissions through Néel and Brownian processes. In addition, susceptibility separation can explain the situation that each relaxation time shifts independently. For instance, when dealing with a non-rotatable matrix (where Brownian motion is controlled), the reaction frequency may shift to the high-frequency region (typically, Néel relaxation occurs much faster).

Next, if Brownian relaxation causes frictional heat, the real part of the Brownian susceptibility (χ'_B) responsible for particle movement should be directly related to the heat calculation. To illustrate this correlation, Fig. 1b shows the initial hysteresis at a real susceptibility of 100 kHz in the MNP schematic. When the susceptibility of each relaxation is determined by the frequency (or measurement time τ_m), the saturation magnetisation of each mechanism can be determined ($M_{S,N}$ for Néel *and* $M_{S,B}$ for Brownian). From the macroscopic view of M_S and $M_{S,B}$, the range of the rotation angle owing to Brownian relaxation can be determined. Additionally, from M_S and $\chi'_B{\cdot}H$, it is possible to predict the average angle of actual rotation relative to the total saturation magnetisation ($-M_S \sim +M_S$, $-180°$ to $+180°$). This angle

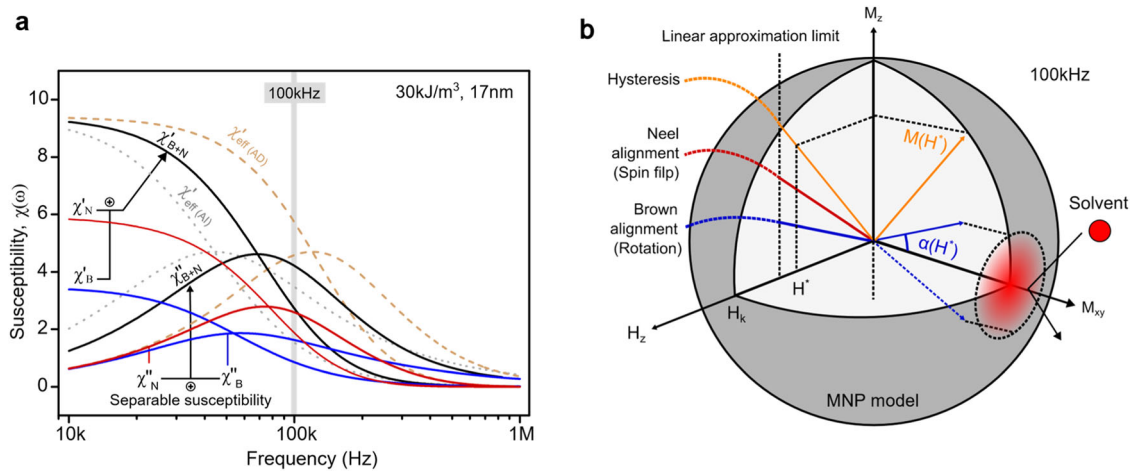

Fig. 1 Mathematical separation of Brownian and Néel susceptibilities for a 1 mg/mL ferrofluid containing 16 nm Fe_3O_4 particles with $K_{eff} = 30$ kJ/m³. The size and frequency were chosen to effectively highlight these differences, and $H{\cdot}f = 5$ kHz·T was used in this calculation. Because both Néel and Brownian relaxation times depend on the amplitude of the magnetic field, amplitude-dependent relaxation models[70] were introduced. **a** Brownian (blue), Néel (red) susceptibilities, and total susceptibility (orange) are expressed with real and imaginary parts; susceptibilities based on Eq. 1 are described with dotted (amplitude-independent, AI) and dashed (amplitude-dependent, AD) lines. **b** Initial hysteresis at corresponding susceptibility at 100 kHz. Magnetisation is represented by the linear product of susceptibility and field amplitude below the LRT limits. The angle α denotes the rotation angle in each MNP, which is inversely calculated from Brownian susceptibility. This rotation directly causes the MNPs to collide with the surrounding solvent, leading to heat generation.

is expressed in Fig. 1b as α ($-\alpha$ ° to $+\alpha$ °), indicating the magnetisation angle, which will be discussed further in later sections.

Therefore, the total volumetric dissipated power of the ferrofluid can be formulated for the two types of power sources using Eq. 3:

$$P_{\mathrm{FF}} = \left(\mu_0 \pi H_0^2 f \chi'' - P_l\right) + P_r = P_{\mathrm{N}} + P_{\mathrm{B}} \tag{6}$$

Therefore, we aimed to determine a mathematical expression that describes P_r, that is, the amount of frictional heat dissipated per unit particle or volume. In the next section, the potential range of dissipated frictional heat caused by Brownian motion is modelled based on χ'_{B}, establishing a mathematical foundation for multichannel resonance in the FFs. Based on these results, a theoretical basis was provided for multichannel resonance in ferrofluids containing two or more mixed-particle types, where each particle operates only within a specified frequency range.

Results

First, we derived a mathematical model to predict the range of frictional power generated by Brownian rotation. The results were compared with the experimental values.

While magnetostrictive effects exist in MNPs[36], our model assumes a continuous alignment of the magnetization vector within magnetic particles along the radius vector. This assumption implies that the axis of magnetostriction changes constantly from the perspective of the crystal lattice. Therefore, we also assumed that averaging these effects over each cycle could neutralize their overall impact.

In this study, the power dissipation values were unified in terms of the specific absorption rate (SAR [W/g_{FF}]), which is closely related to the theoretical mechanism of both relaxation processes, considering that solvents also play an important role in Brownian heat generation. In this study, we adopted both the empirical Brownian relaxation model proposed by Yoshida and Enpuku[37] (Eq. 7) and the Néel relaxation model proposed by Chalifour[38] (Eq. 8), both of which depend on the field amplitude. Details on these model selections are provided in Supplementary Methods 1.

$$\tau_{\mathrm{B,H}} = \frac{3\eta V_{\mathrm{h}}}{k_{\mathrm{B}} T \sqrt{1 + 0.126\xi^{1.72}}} \tag{7}$$

$$\tau_{\mathrm{N,H}} = \frac{\mu_0 M_{\mathrm{S}}}{4\gamma K_{\mathrm{eff}}} \frac{1+\alpha_{\mathrm{d}}^2}{\alpha_{\mathrm{d}}} \frac{\cos(\sin^{-1} h)}{\sqrt{1-h}(1-h^2)} e^{\sigma(1-h)^2} \tag{8}$$

The blocking temperature (T_{B}) of the MNPs was calculated using Eq. 8 (See supplementary Fig. 1). Specifically, we focused on assessing the thermal utility of Fe_3O_4 nanoparticles by adjusting K_{eff} via doping with other elements or by introducing exchange boundaries. To comprehensively evaluate their activation, we used a unified density (ρ) along with magnetic properties such as the saturation magnetisation (M_{S}), g-value (g), damping constant (α_{d}), and gyromagnetic ratio (γ) of the ferrite

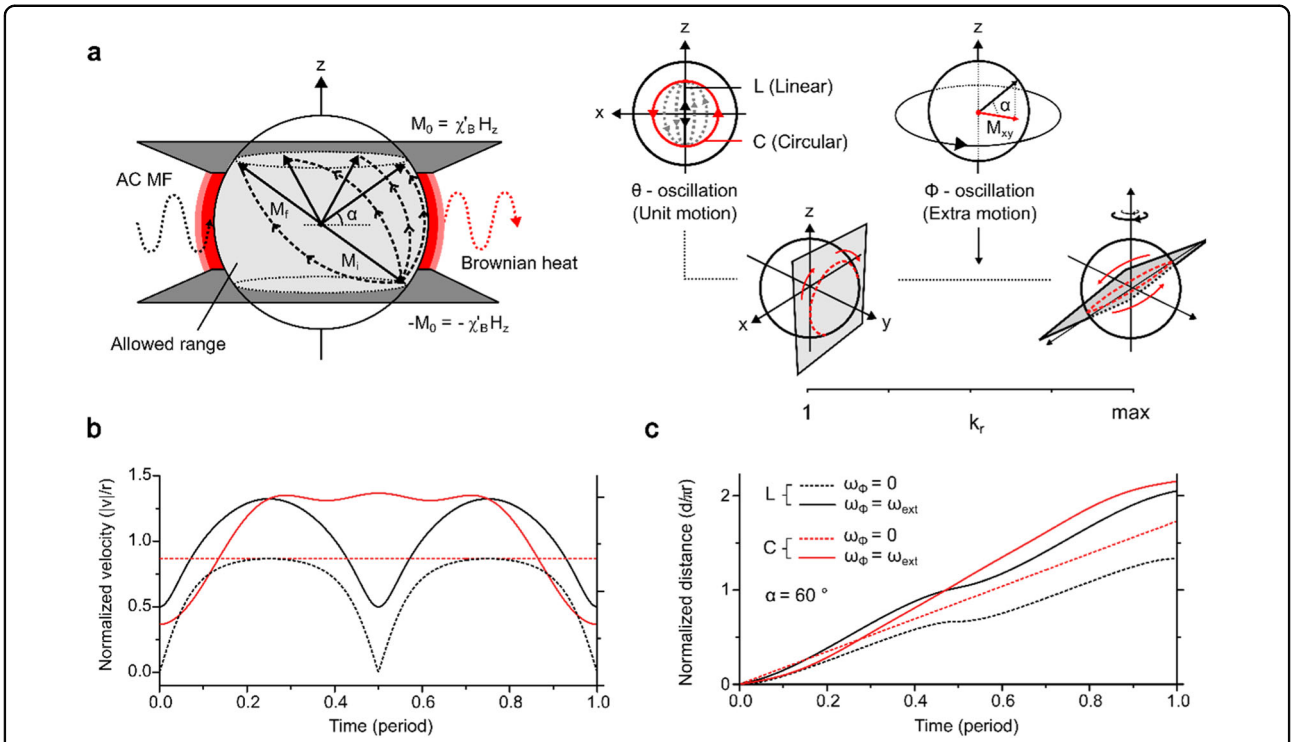

Fig. 2 Conceptual framework of the Brownian dissipation model. a The z-component of magnetisation is constrained along the radius vector and limited within the range allowed by the Debye equation. Additional motions adhering to this deterministic z-constraint can introduce stochastic contributions, resulting in a periodic trace of the normal (radius) vector that dissipates energy steadily without deviating from the z-magnetisation path. **b** Comparison of cases with stochastic rotational components (solid lines) and without additional motion (dashed lines, where only unit motion exists) over one cycle for the velocity of a point on the particle surface, with α = 60 °. Notably, in linear unit motion without additional ϕ-oscillation, the magnetic nanoparticle (MNP) should stop and rotate 180 ° to realign, as shown by the black dashed line. **c** Comparison of cases over one cycle for the displacement of a point on the particle surface, with α = 60 °.

particles. Additionally, as the particle size increases, the rate of change in K_{eff} diminishes due to the interparticle interaction, with 5 mg/mL FF in the 10–20 nm range showing less than 2% variation[39] (Supplementary Fig. 2). As a result, a detailed discussion on interparticle interaction effects has been excluded in this model. However, future investigations following this framework could further delve into how these interactions influence heat generation to arrive at a conclusive inference.

Brownian Dissipation model and thermal analysis

To deduce a rational equation for frictional power dissipation in Brownian rotation, we began by estimating the trace of the radius vector, which moved along with the magnetisation vector of the magnetic particles. The heat generated can be calculated by estimating the rotation of the particles relative to the solvent. However, there is a limited way to directly determine the extent to which the particles rotate relative to the solvent because we can only externally measure the temperature. Therefore, we calculated the theoretical "range" of heat by considering the minimum and maximum traces of the particles under ideal conditions, and then approximated the actual trace of the particle using the experimental value, as long as the particle did not violate the Debye model within a given magnetic field. Because z-magnetisation (M_z) is defined by the Debye model, a possible periodic trace of the radius vector that obeys the z-constraint was expressed (Fig. 2a). Here, we provide a range of rotations using simple modelling described below:

Let us assume that N magnetic particles, which have the same core, hydrodynamic volume, and composition, are well dispersed in a solvent with viscosity η. The centres of the particles are fixed at certain points, and the magnetisation of each particle is 'frozen' at itself such that particle rotates along with the magnetisation under Brownian relaxation. Then, the collective motion of particles can be understood as a trace of a magnetisation vector: when magnetisation itself is positioned at (0, M_0, 0), and a uniform AC magnetic field $\mathbf{H}(t) = \mathbf{k}H_0 \cdot \cos(\omega_{ext} t)$ is applied along the z-axis, the resulting

expectation value of z-magnetisation can be expressed as

$$\mathbf{M}_z(t) = \hat{\mathbf{k}} M_0 \cdot \cos(\omega t - \delta) = \hat{\mathbf{k}} M_S \cdot \left[\frac{\chi'_B H_0}{M_s} \cos(\omega t - \delta)\right] \tag{9}$$

Because $0 \le \chi'_B \cdot H_0 / M_S \le 1$, it can be replaced with a sine value of angle α, which implies the magnetisation angle (Fig. 1b):

$$\mathbf{M}_z(t) = \hat{\mathbf{k}} M_S \cdot [\sin\alpha \cos(\omega t - \delta)] \tag{10}$$

This substitution simplifies the mathematical calculations. The total z-radius vector of the particles in FF is given by

$$\boldsymbol{r}_{z,\mathrm{FF}}(t) = \sum_{i=1}^{N} \boldsymbol{r}_{z,i} = \hat{\mathbf{k}} N r_h \cdot [\sin\alpha \cos(\omega t - \delta)] \tag{11}$$

where r_h is the hydrodynamic radius of the magnetic particles. In the classical way, this collective vector can be thought of as the sum of N average radius vectors of the particles, that is, $\boldsymbol{r}_z(t) = N \cdot \boldsymbol{r}_{z,\mathrm{avg}}(t)$, and the averaged expected radius vector of each particle can be expressed as follows:

$$\mathbf{r}_{z,\mathrm{avg}}(t) = \hat{\mathbf{k}} r_h \cdot [\sin\alpha \cos(\omega t - \delta)] \tag{12}$$

Regardless of the phase lag, the values of $\boldsymbol{r}_{z\ and\ avg}(t)$ oscillate with a cosine function. This implies that the group of immersed particles exhibited at least one periodic motion (θ-oscillation, denoted as "unit motion"), even when subjected to complex motions involving thermal collisions and rotation by magnetic potential energy. Therefore, another motion must be superimposed on the system that does not violate the theoretical equation or experimental observations of M_z. This motion (ϕ-oscillation, denoted as "extra motion") could be related to thermal collisions or other magnetic effects, such as precession.

To explore another motion that satisfies the r_z constraint, it is intuitive and mathematically useful to assume that it is periodic in a continuous AC field. This allowed us to estimate the range of rotation distances and frictional heat caused by Brownian relaxation. Based on this assumption, we modelled the particle motion as the sum of two periodic motions: one representing the unit motion that expresses the z-oscillation, and the other encompassing all the remaining effects combined, as illustrated in Fig. 2a.

Initially, the unit motion fundamentally could be conceptualised as linear motion (L) along the axis. However, this assumption requires the radius vector to halt twice per cycle to rotate 180 °, introducing discontinuities in the motion. While this concept remains plausible at frequencies significantly below the resonant frequency where the heating is inefficient, it becomes increasingly untenable as the frequency approaches resonance.

To overcome this limitation, we proposed that the maximum feasible motion of the unit motion is circular (C). This assumption provides a continuous trajectory without abrupt stops, consistent with the physical constraint that the radius vector oscillating in the z-direction cannot produce greater displacement in the xy-direction than along the z-axis.

Following the same principle, we further constrained the extra motion by assuming that its rotation frequency would not exceed the unit motion frequency ($0 \le \omega_\phi \le \omega_{ext}$). This prevents the unphysical scenario where extra motion rotates more than once per cycle of the unit motion.

Further, we can assume that the solvent particles surrounding the MNPs, particularly those on the hydrodynamic surfaces of the magnetic particles, are either at rest or cohesively translated with the solvent. This implies that the relative vorticity was zero ($\Omega = 0$). Even when the solvent moved during translation with the particles, it did not exhibit any rotational movement with respect to the particles. Consequently, Stokes' law can be applied to calculate the frictional heat.

$$\begin{aligned}\langle Q \rangle &= \int_0^{2\pi} f_r d\theta = \int_0^{\frac{2\pi}{\omega}} 8\pi\eta r^3 (\Omega - \omega) \cdot (\Omega - \omega) dt \\ &= 6\eta V_h \int_0^{\frac{2\pi}{\omega}} \{\omega(t)\}^2 dt\end{aligned} \tag{13}$$

In this context, f_r is the frictional force during rotation. The range of heat dissipated by friction per cycle can be calculated using Eq. 13. To integrate these calculations, we set a basis point corresponding to a circular trace (C) of θ-rotation and $\omega_\phi = 0$, which can be easily calculated. In turn, the mathematical equation of frictional heat generated by a single particle can be expressed simply by multiplying the rotary coefficient k_r ($k_r \le 0.5 + (\sin^2\alpha)^{-1}$) based on this basis point, expressing their ratios and range. Therefore, the total volumetrically dissipated Brownian heat from the ferrofluid can be calculated as

$$\begin{aligned}P_B[\mathrm{W/m^3}] &= \frac{Nf\langle Q \rangle}{V_{\mathrm{FF}}} = 6n\eta k_r V_h \omega^2 \sin^2\alpha \\ &= 6n\eta k_r V_h \left(\omega \frac{\chi'_B H_0}{M_s}\right)^2\end{aligned} \tag{14}$$

N (number of particles) and V_{FF} (volume of ferrofluid) were reduced to n (number density). Additional details between Eqs. 13 and 14 are provided in Appendix A. Based on Eq. 14, we developed a refined version of the dissipation model for the FFs that reflects the heat

generated by Brownian rotation, as follows:

$$P_{FF}[W/m^3] = P_N + P_B = \mu_0 \pi H_0^2 f \chi_N'' + 6n\eta k_r V_h \left(\omega \frac{\chi_B' H_0}{M_s}\right)^2 \quad (15)$$

$$SAR[W/g] = c_{FF} m_{FF} \cdot \left(\frac{dT}{dt}\right)_{initial} \quad (16)$$

where c_{FF} and m_{FF} represent the specific heat (J/K·g) and mass (g) of the ferrofluid, respectively, which were calculated as the average values based on the solvent-to-particle ratio. Subsequently, both the theoretical SAR values are presented based on the conventional model (Eq. 2, SAR_R) and the SAR derived from our work (Eq. 15), which are separated into spin-lattice interactions (Néel, SAR_N) in red and rotational friction (Brownian, SAR_B) in blue, along with the experimental values. The measured temperature reached a steady state after approximately 90 s, which marked the end of the heating phase in the experiment[40] (Supplementary Fig. 3).

Although the actual heat largely deviated from the theoretical values of SAR_R and SAR_B (where $k_r = 1$), the experimental k_r values were 357.1 ± 53.9 at 18 mT, 321.29 ± 53.9 at 24 mT, and 321.29 ± 53.9 at 27 mT. Furthermore, smaller particles or those with low K_{eff} values, which were theoretically expected to generate negligible heat at 104 kHz in both theories, did not produce measurable heat (see supplementary Fig. 4 and 5). Although the fabricated MNPs in FF appeared monodispersed (Supplementary Fig. 6), approximately 8% particles underwent soft agglomeration in the solvent during the experiment (Supplementary Fig. 7), as characterized by a hydrodynamic volume of approximately 128 nm diameter. Given that softly agglomerated particles experience friction within the cluster under the applied magnetic field, this friction is expected to be slightly less than that of individual particles[41–44]. Therefore, this experimental value may be slightly greater, indicating a greater deviation from the conventional analysis.

Notably, the calculated SAR_R and SAR_B (with $k_r = 1$) were significantly lower than the experimental values for the FFs containing Brownian rotation-accepted particles (Co-doped particles). Interestingly, the observed motion was, on average, 378.04 ± 56.1 times larger than the theoretical circular unit motion. This finding demonstrates that the previous heat equations inherently underestimated the contribution of Brownian heat. Furthermore, the idea of unit motion (where $k_r = 1$) can be directly converted into angular terms (α), offering an intuitive interpretation (Fig. 3c).

Furthermore, we observed that the experimental Brownian heat increased rapidly at the experimental field values. Although assuming that the heat generated by the FF does not surpass the maximum value set by us, this heating value must eventually saturate. To model this behaviour, we fitted the experimental data to an empirical sigmoid function[45,46], considering the experimental values and point (0 mT, 0 W/g_{FF}) on the graph, as in other theoretical[47] and experimental[48] works. The threshold field amplitude H_{th} in the logistic fit was determined as 29 mT, representing the field value at which the generated heat reaches half of the maximum value at 0 mT ($SAR_{B,max}$ shows only slight variation−−approximately 0.08 W/g_{FF} difference between 1 mT and 75 mT, corresponding to about 4%−−i.e. it remains nearly constant).

Therefore, the overall behaviour of Brownian thermal transduction can be understood as occurring in two phases based on H_{th}: an initial increasing phase (low amplitude) and a subsequent saturating phase (high amplitude). During the initial phase, the magnetic energy gradually overcomes the thermal interference, leading to an exponential reversal of magnetisation[49,50]. In the saturating phase, the rate of heat generation gradually slows down within the framework of LRT, which does not account for magnetic saturation. This behaviour can be attributed to the reduced difference between SAR_B and $SAR_{B,max}$, as indicated by the continuous decline in $k_{r,max}$, eventually converging to 1 (Fig. 3d). This reflects how, as the trace of unit motion increases, the relative contribution of extra motion diminishes. Furthermore, the relaxation time reduces at higher amplitudes, which makes the particle more susceptible at high frequencies, thereby reducing Brownian susceptibility (χ'_B). This reduction in χ'_B, combined with the narrowing motion trace, collectively drives the saturation to $SAR_{B,max}$ at those frequencies. This effect becomes more pronounced at lower frequencies ($\omega_{ext}\tau_B < 1$) and for particles with lower K_{eff}. For example, in this study, to achieve a reduction in SAR at 104 kHz, particles with a minimum size in the Brownian region require a field strength greater than 161 mT (53.4 kJ/m^3), and those with higher K_{eff} require over 484 mT (168.1 kJ/m^3). As particle size increases, the critical field strength also increases, exceeding the amplitude range typically used for AC stimulation (1–100 mT, Eq. 7).

SAR analysis and size dependency

The differences in the SAR values for each particle are shown in Fig. 4. The k_r value is predicted to vary depending on factors such as composition, size, and shape. To address this issue, the average k_r values derived from experimental results were utilized for the comprehensive size analysis. In Fig. 4a, the maximum potential SAR (SAR_{max}) was calculated for Fe_3O_4 (K_{eff} = 53.4 kJ/m^3) and $Co_{0.6}Fe_{2.4}O_4$ core-shell particles (K_{eff} = 168.1 kJ/m^3).

Each particle exhibited an initial hump and sharp valley, followed by a gradual increase in both models (Fig. 4a).

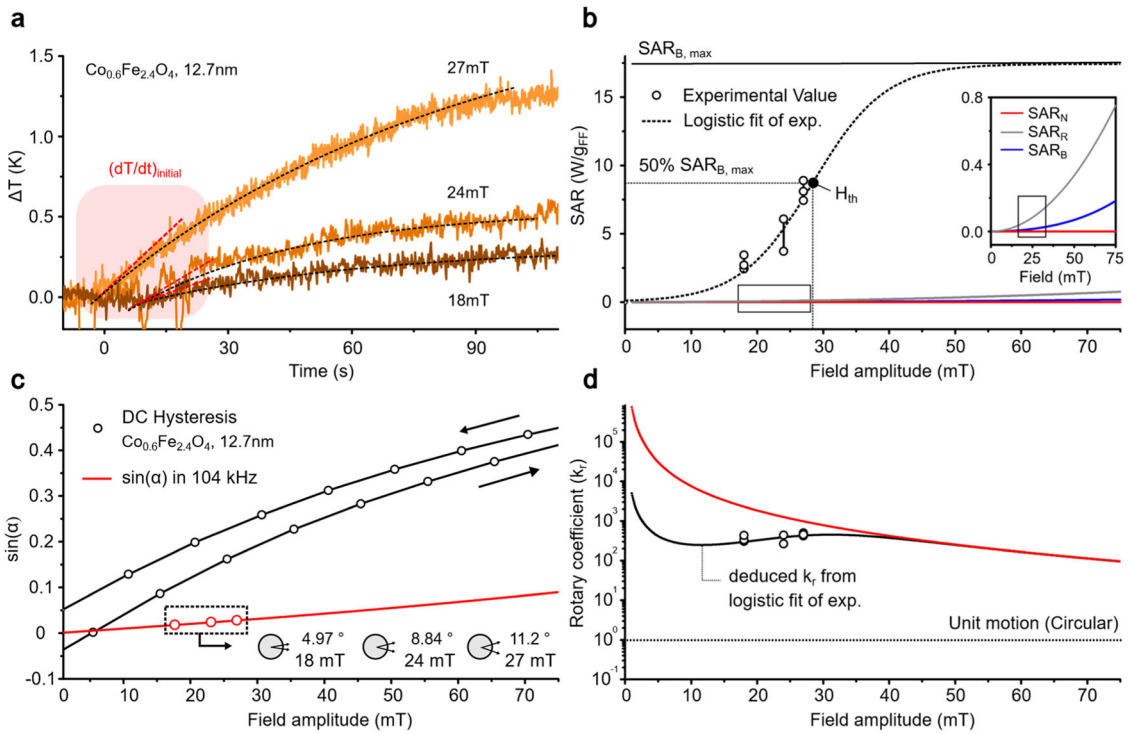

Fig. 3 Trace analysis of radius vector and temperature measurements for magnetic particles. All experiments were conducted using 5 mg/mL FF, composed of 12.7 nm $Co_{0.42}Fe_{2.58}O_4$@$Co_{0.65}Fe_{2.35}O_4$ MNPs (overall composition is $Co_{0.6}Fe_{2.4}O_4$, $K_{eff} = 168.1$ kJ/m^3) dispersed in hexane. **a** The 9-pixel average temperature profile of FF NPs activated at 104 kHz, fitted with the Box-Lucas function. **b** Comparison of the theoretical and experimental SAR values of FF. SAR_R denotes the calculated value based on the conventional model by Rosensweig, and SAR_N (Néel) and SAR_B (Brownian) are the calculated values from this work. Subsequently, logistic fitting was performed with the sigmoid function. H_{th} represents the value of H at which the fitted function reaches half of its maximum predicted value. **c** Plot of sin(α) as a function of the applied field amplitude, compared with the DC hysteresis value (black), illustrating the oscillation angle along the z-axis at 104 kHz. **d** The maximum rotary coefficient ($k_{r,max}$) where $\omega_\phi = \omega_{ext}$ and the rotary coefficient deduced from a fitted logistic curve are represented.

This hump arises from heat from Néel relaxation[51], whereas the gradual increase is attributed to Brownian relaxation[52,53]. A sharp transition from the Néel-dominated to Brownian-dominated regions was observed with increasing particle size, where both mechanisms operated simultaneously. In this region, SAR_{max} values were measured across a wide range of frequencies (Fig. 4d), spanning from 100 kHz to approximately 3 MHz, while Brownian (<100 kHz) or Néel (~3 MHz) relaxation remained almost stationary.

First, the Néel hump indicates that relatively small particles tend to generate heat through Néel relaxation but have an optimum size range for maximum efficiency when $H{\cdot}f$ is constant. In addition, notably, lower K_{eff} values resulted in higher and broader SAR_{max} peaks at higher frequencies when comparing the two different FFs. Therefore, when stimulating particles at high frequencies for Néel relaxation (e.g., in environments where particle movement is restricted, such as cellular uptake[9]), it is crucial to use particles with a lower K_{eff} that are as large as feasible. However, if the goal is to stimulate a mixture of various particles at the same time for frequency-sensitive multiplexed activation, a higher K_{eff} would be advantageous. Particles with a higher K_{eff} offer better sensitivity, meaning that they can turn off well at other frequency channels, although they might not be efficient transducers.

The heat generated by Brownian relaxation also increased in both models (previous model and our work). In the larger-sized region, the SAR_{max} of each particle begins to converge, implying that Brownian dissipation depends only on the size itself. However, compared with the conventional model (dashed line), the measured SAR_{max} from the Brownian relaxation was much higher than that of the existing theory. This difference supports the rationale for multichannel activation, which is explained later.

Finally, as the dominant mechanism transitioned from Néel relaxation to Brownian relaxation with increasing particle size, a sharp valley appeared between the two regimes. The lowest point of this valley was where the heat from each mechanism was the same. Beyond this

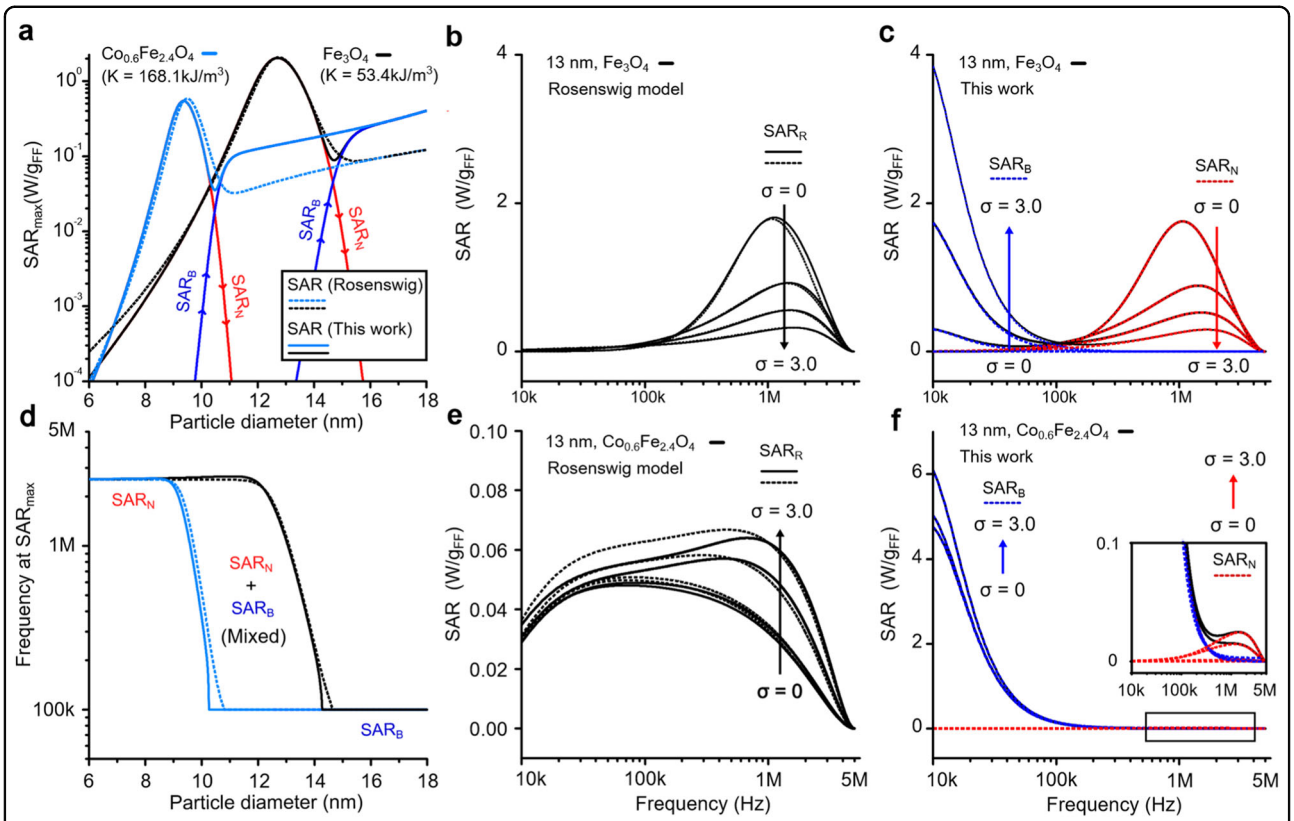

Fig. 4 Calculation of SAR values. All calculations were performed with 5 mg/mL FFs dispersed in water and $H{\cdot}f = 3$ kHz·T, which is below the biomedical safety limits. The rotary coefficient (k_r) of Brownian heat was set to 378.04, which was deduced from the average of the experimental values. The mean particle size of the FFs was 13 nm, with a standard deviation(σ) ranging from $\sigma = 0$ (monodisperse) to $\sigma = 3$ nm. The calculations were categorised into two regions: Néel-relaxing Fe_3O_4 (**b**, **c**) and Brownian-relaxing Co-doped particles (**e**, **f**), based on the conventional model and our model, respectively. **a** Maximum potential SAR value (SAR_{max}) for each particle size (6–18 nm). **b** Calculation of SAR value for 13 nm Fe_3O_4 particles using the Rosensweig model, and **c** calculation using our model. **d** Corresponding frequency at SAR_{max} for each particle size (6–18 nm). Frequencies below 100 kHz are quenched, to accurately describe the overall behaviour under the condition of constant $H{\cdot}f$. **e** Calculation of the SAR value for 12.7 nm $Co_{0.6}Fe_{2.4}O_4$ core-shell particles with the Rosensweig model and **f** using our model.

point, the spin reversal energy ($\sigma = K_{eff}V/k_BT$) increases with particle size, making Brownian relaxation more feasible. The resonant frequency continuously shifted to a lower frequency band, and at the bottom of the valley, the frequency fell within the Brownian regime. Although both mechanisms were inefficient in this transitional section, they dissipated thermal energy simultaneously. This triangle-shaped area made of SAR_B and SAR_N is important because it has the potential for generating maximum heat at frequencies between the two distinct zones (Fig. 4d). If particles in this region are used, multiplexed activation using two, three, or more channels is possible.

Next, the SAR for the FFs containing the size distribution of MNPs was calculated using both models. Unlike the conventional models (Fig. 4b, e), our model (Fig. 4c, f) allows for the separation of SAR_N and SAR_B, enabling a more detailed analysis of the size distribution with respect to each relaxation mechanism. For the Néel-relaxing particles (Fig. 4b, c), the calculated heat decreased as the sample became more polydisperse, particularly in the high-frequency region. This phenomenon arises from the significant number of particles deviating from the peak (Fig. 4a) where efficient Néel relaxation occurs. Regardless of the average particle size, it is evident that the number of particles at the optimal size is crucial for achieving maximum efficiency, in both models. Moreover, a larger size distribution resulted in emerging the Brownian peak in the low-frequency region. Therefore, when used simultaneously with Brownian particles for the effective on-off based on frequency, it is best to use particles that are as monodisperse as possible to create the FF.

In contrast, for particles undergoing Brownian relaxation (Fig. 4e, f), the calculated amount of heat exhibits relatively minor variation and even increases, indicating that larger-than-average MNPs contribute more to heat generation than their smaller counterparts. Moreover, the response frequency broadened with increasing size distribution as particles of different sizes contribute to the

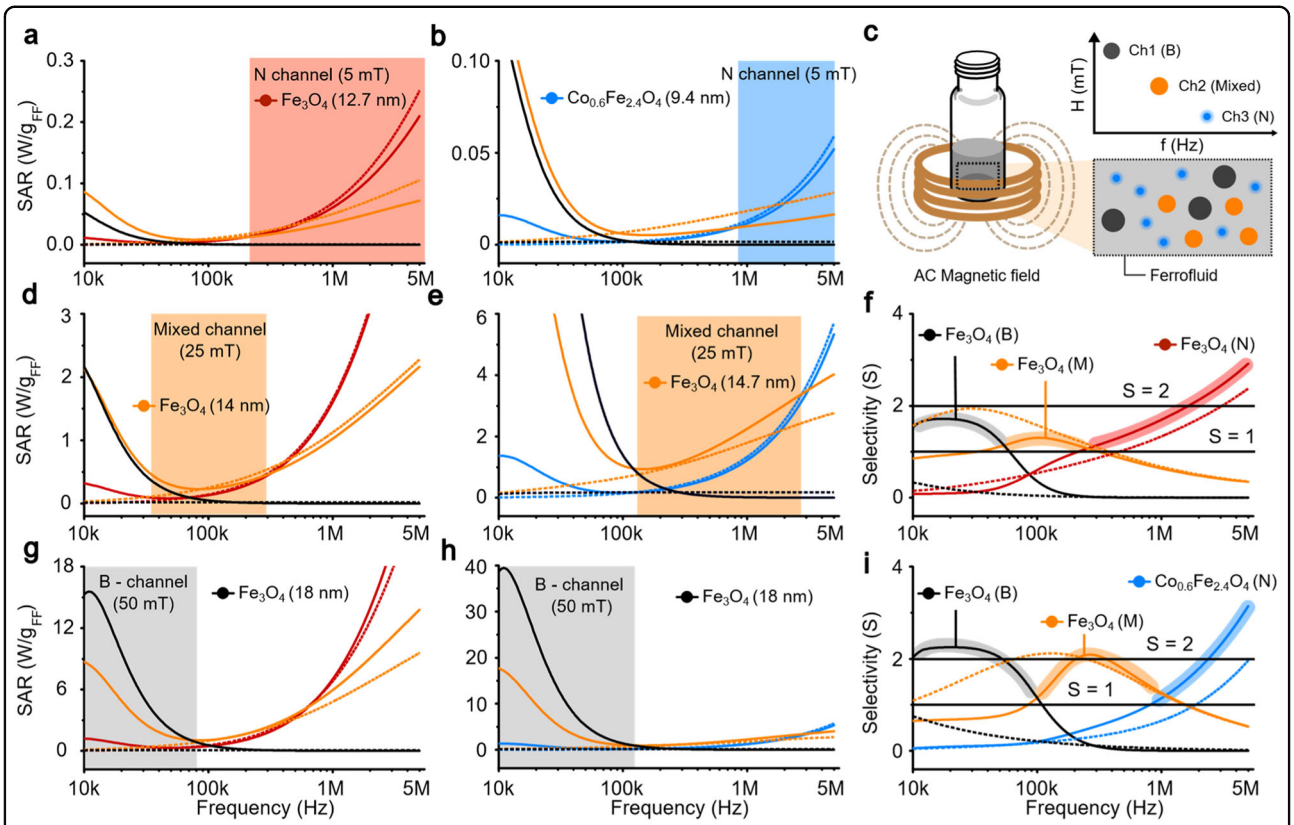

Fig. 5 Theoretical possibility of 3-channel activation ($H{\cdot}f = 3$ kHz·T) using three different particles. All calculations were performed with FFs containing three particle types ($n = 1000$ for each), each with a standard deviation of 1 nm, dispersed in water. Two types of FFs were analysed: FF-1 and FF-2. FF-1 (**a**, **d**, and **g**) contains only Fe_3O_4 particles with different sizes: N channel (12.7 nm, 10 mg/mL), M channel (14 nm, 10 mg/mL), and B channel (18 nm, 1 mg/mL). FF-2 (**b**, **e** and **h**) contains both pure Fe_3O_4 and $Co_{0.6}Fe_{2.4}O_4$ core-shell particles: N channel (9.4 nm, 10 mg/mL), M channel (14.7 nm, 7.5 mg/mL), and B channel (18 nm, 2.5 mg/mL). Each particle is distinguished by a different colour. The dashed lines indicate calculations using the Rosensweig model for each particle. **a** SAR of FF-1 and **b** FF-2 at 50 mT, stimulating the N channel. **c** Main idea of 3-channel activation. **d** SAR of FF-1 and **e** FF-2 at 25 mT, stimulating the M channel. **f** Calculated channel selectivity of FF-1, by $S_n = P_n / (\sum P_n)$. **g** SAR of FF-1 and **h** FF-2 at 50 mT, stimulating the B channel. **i** calculated channel selectivity of FF-2.

heat generation at slightly different resonant frequencies. Notably, a larger size distribution led to the emergence of the Néel peak in the high-frequency region. Thus, while Brownian power is less sensitive to size distribution than Néel-relaxation particles, achieving a narrow size distribution remains advantageous for optimising multiplexed stimulation.

Channel selective activation analysis

By rationally utilising the characteristics of MNPs, the distinctive channels of their FFs can be used to effectively adjust their turn-off and turn-on states by tuning the external frequency of the magnetic field. Beyond 2-channel activation, the existence of 3-channel activation has been confirmed experimentally[54]. However, it was not possible to theoretically verify this phenomenon using previous approaches. Our approach provides a theoretical basis for verifying selective activation, even with three channels, thereby enhancing the precision and effectiveness of multichannel magnetothermal applications, as shown in Fig. 5.

In Fig. 5c, a schematic diagram of the 3-channel activation is presented. Regardless of how the FFs were fabricated (e.g., three different FFs or a single FF containing three different MNPs), when every particle was under the same magnetic field, each particle generated heat to its capacity.

Channel activation can be realised in the Brownian (B), Néel (N), and mixed (M) relaxation regions. There were a total 10 possible combinations (B/B/B–N/N/N) in three channels. First, the frequency–dependent heating morphology at same H must be considered when designing the MNP mixture. Channel B peaked at low frequencies and then turned off, whereas channel N generated more heat at higher frequencies. Channel M has a small capacity in both regions but forms the most heat in the overlapping intermediate region when H is constant ($H{\cdot}f$ is linearly increasing). Given the intrinsic dissipation

forms of each relaxation mechanism, using the Brownian(B), Néel(N), and mixed (M) relaxation channels individually is an efficient approach for three-channel activation, as previously mentioned. To implement each channel in the simplest manner, a method that utilises a single type of particle of different sizes can be used. Therefore, the heat from Fe_3O_4 particles of different sizes was measured in magnetic fields of three different intensities to determine the separated regions of their respective maximum regions at each intensity (Fig. 5a, d and g). Since the Brownian heat is significantly greater than the Néel heat, the concentration of the N channel was adjusted to be higher than that of the B channel for practical applications.

Additionally, the selectivity (S) was calculated for each channel: 5 mT for the N channel, 25 mT for the M channel, and 50 mT for the B channel. First, when the selectivity was calculated using the Rosenzweig model, no cases were found where all channels exceeded $S > 1$. This implies that the theoretical establishment of the three channels is not feasible with the existing theory.

In contrast, our model demonstrates that each channel exceeds $S > 1$ at different, non-overlapping frequency ranges. Moreover, neither the existing theory nor our model demonstrates an $S > 2$ region for all three channels. This means that although iron oxide particles can exhibit the behaviour of the three channels, they are not remarkably selective, even when nearly monodispersed (1 nm standard deviation).

Since single particle 3-channel activation does not exhibit remarkable selectivity, it becomes necessary to substitute them with other particles to enhance the selectivity. In this context, the most challenging task is securing selectivity of M-relaxation channel. To achieve this, it is crucial to use N- or B-channel particles with the narrowest possible channel widths. This ensures that the particles contributing to each relaxation mechanism are sufficiently distinct to avoid overlap, thereby enhancing the selectivity of the channel activation approach. Since the B channel is solely size-dependent and thus difficult to adjust, it is preferable to shift the N channel to secure the M channel. This can be accomplished using large K_{eff} particles as channel N (Fig. 5b, e, h). Replacing the Néel particles with a high-K_{eff} material results in a shift to a higher, narrow frequency band.

In this scenario, it is advantageous to use low-K_{eff} particles for channel M. This is because, as the Néel hump increases (Fig. 3a), the bottom point of the mixed relaxation also remains at a higher value. Therefore, this strategy can also enhance selectivity by increasing the amount of heat in the mixed relaxation. This technique ensured an area in which the mixed channel could operate, as shown in Fig. 5b, e, and h. As shown in Fig. 5a and b, when using this cobalt-doped Néel channel, the frequency at which the N channel achieved maximum heat generation shifted from the >300 kHz to >1 MHz range, enhancing the selectivity in the mixed channel within this region. Simultaneously, this modification also enabled the realization of $S > 2$ across all channels (Fig. 5i), overcoming the limitations of iron oxide particles alone.

In particular, when multiplexed activation is used, it is unlikely that each particle simultaneously occupies the same location (generally, the aim is to stimulate different parts). Therefore, if the magnetic field is concentrated in each part (preventing it from affecting other regions), the channel selectivity of heat from the particles can be further guaranteed. However, if the frequency selectivity of the particles is improved, selective stimulation is possible even in smaller areas (even in areas where the magnetic field is difficult to separate).

Discussion

In this study, the Brownian dissipation model was employed to focused on understanding the extent to which heat production deviates from established theoretical knowledge, rather than attempting to capture the exact complex motion of the particles, with an aim to refine the previous approach. By integrating this model, we achieved a more accurate prediction of the heat generated by the Brownian rotation of magnetic nanoparticles (MNPs). This refinement enabled a more precise differentiation between the heat contributions from the Néel and Brownian relaxation mechanisms. Additionally, the theoretical exploration of three-channel activation using different particles highlights the potential for selective heating, enhancing the precision of multimodal therapeutic strategies. This approach could replace the traditional treatments used in neurodegenerative brain diseases, such as electrical stimulation or deep brain stimulation (DBS). Moreover, its compact size gives the unique advantage of enabling the wireless observation of dynamic synaptic plasticity, a feature that has been challenging to achieve with large-sized implant-based devices.

Precise neuron-by-neuron targeting by Brownian-based treatment remains a substantial hurdle. While strategies using viral vectors or antibodies can facilitate cell- or protein-specific targeting[55], they hinder the Brownian rotation of MNPs, compromising the efficiency of heat generation. Furthermore, as this technique is thermally driven, successive stimulation is constrained because it necessitates waiting for cooling before reapplying the stimulus.

Despite these inherent limitations, the use of solutions with three or more channels including Brownian MNPs provides the “degrees of freedom” in the injected sites, as if the injection area is effectively divided according to the number of channels. This implies that even with

randomly distributed MNPs, as long as the particles corresponding to each channel are located in different areas, distinct neurons can be stimulated by each channel, irrespective of their exact locations. This design idea facilitates the potential for broad, complex stimulation patterns with complex imitation of neural dynamics, such as sparse coding, observed in sensory[56] or memory[57] circuit.

Additionally, achieving optimal Brownian motion requires perfectly monodisperse particles without coating layers, as any coating increases the distance between the magnetic torque and the point of frictional force, further diminishing rotational efficiency. This directly complicates the quantitative determination of k_r which may depend on various factors such as temperature, particle size, anisotropy, surface coating, and solvent viscosity. Our results indicate that analysing the trends in k_r across different types of particles could further refine our equations and improve the predictive accuracy of heat generation models.

In conclusion, the incorporation of the Brownian dissipation model into heat generation calculations offers a robust framework for optimising MNP-based therapies. This study highlights the importance of particle size, distribution, and magnetic properties in maximising therapeutic outcomes, thereby advancing the field of magnetothermal energy conversion and its biomedical applications. This approach supports precise neuromodulation, in which spatial selectivity and controlled activation are critical.

Methods

The reagents, apparatus are detailed in Supplementary Methods 2, and characterisation procedures are shown in Supplementary Figures.

Preparation for Fe_3O_4 nanoparticles

Following a typical procedure[58,59], iron acetylacetonate (1.059 g, 3 mmol), 1,2-hexadecanediol (4.706 g, 15 mmol), oleic acid (OAc; 4.706 g, 15 mmol), oleylamine (OAm; 5.732 g, 15 mmol), and benzyl ether (30 mL) were added. Although stoichiometric calculations appear to require only 9 mmol of OAc and OAm, a substantial amount of OAm can facilitate the synthesis of larger nanoparticles[60–64]. This mixture results in Fe_3O_4@Fe_3O_4 nanoparticles with an average size of 13.2 nm and a standard deviation of 0.96 nm (Supplementary Fig. 6), after the two-step synthesis.

Preparation for cobalt-doped nanoparticles

When iron acetylacetonate was reduced to 2 mmol, cobalt acetylacetonate (0.257 g, 1 mmol) was added. In this case, decomposition temperature of $Co(OL)_2$, the precursor produced during synthesis, is higher than that of $Fe(OL)_3$[65], so a higher doping concentration can be achieved at higher temperatures. Therefore, through a one-pot, two-step growth, we achieved a $Co_{0.42}Fe_{2.58}O_4$@$Co_{0.65}Fe_{2.35}O_4$ core-shell structure with an average size of 12.7 nm and a standard deviation of 1.13 nm (Supplementary Fig. 6).

One-pot seed-mediated growth method for anisotropy engineering

Fe_3O_4@Fe_3O_4 and $Co_{0.42}Fe_{2.58}O_4$@$Co_{0.65}Fe_{2.35}O_4$ (overall composition of $Co_{0.6}Fe_{2.4}O_4$) nanoparticles with average core sizes of ~8 and ~5 nm, respectively, were synthesised via a one-pot two-step thermal decomposition method. Controlling the size is crucial in our work, which is why we chose thermal decomposition because it offers advantages in this regard[66–68]. In addition, controlling the anisotropy constant (K_{eff}) is important for achieving Brownian relaxation. Therefore, we were able to effectively change K_{eff} by changing its composition and creating a core-shell structure[69] through the seed-mediated growth of that particle.

Each precursor was placed in a three-neck flask and stirred at 300 rpm for 10 min to obtain a homogeneous mixture. The temperature was then raised to 110 °C for 1 h to eliminate moisture and extra moieties, such as acetylacetone (Hacac), which is formed during ligand exchange from acetylacetonate to OAc[63]. During this period, nitrogen gas was introduced into the mixture at a flow rate of 100 sccm to maintain an inert atmosphere. The temperature was further increased to 190 °C at a heating rate of approximately 10 °C/min, and the mixture was refluxed for 1 h to fabricate a core with an approximate size of 8 nm (Supplementary Fig. 5). After core synthesis, the temperature was increased again to 290 °C at a heating rate of approximately 3.3 °C/min, and the mixture was refluxed for an additional hour to generate a shell around the core.

Acknowledgements

This study was supported by the Bio Medical Technology Development Programme through the National Research Foundation of Korea (NRF), funded by the Ministry of Science and ICT [2022M3E5E808120212], and a National Research Foundation of Korea (NRF) grant funded by the Korean government (MSIT) [2020R1A5A101913111].

Author contributions

M.S. and D.K. proposed the research concept and designed the experiments. The research framework and methodology were developed by M.S., D.K., D.P. and J.K., with H.C. serving as the project investigator. M.S. conducted the theoretical modelling, computational analysis and multichannel evaluation. The synthesis procedures and material characterizations were carried out by M.S., D.K. and J.H., while M.S., D.K., J.H. and M.H. contributed to the thermal characterization and analysis. M.S. prepared the manuscript and figures. All the authors reviewed and approved the final manuscript.

Data availability

The datasets generated and/or analysed during the current study are available from the corresponding author on reasonable request.

Competing interests
The authors declare that they have no conflicts of interest. The authors have no competing financial interests or personal relationships that could have influenced the work reported in this study.

Ethics approval and consent to participate
This research, based on computational materials simulations, adheres to the principles of scientific integrity and was conducted in accordance with the highest standards of research ethics and data management.

Publisher's note
Springer Nature remains neutral with regard to jurisdictional claims in published maps and institutional affiliations.

Supplementary information The online version contains supplementary material available at https://doi.org/10.1038/s41427-025-00587-7.

Appendix A

Derivation of P_B

Here, we introduce the detailed steps for the calculation of P_B, resulting in Eq. 14.

If $\boldsymbol{r}_{av}$ is initially positioned at $r(0, \cos(\alpha), \sin(\alpha))$, the two extreme cases of unit motion of the radius vector (linear and circular, denoted as L and C, respectively) can be expressed when $H_0 \cdot \cos(\omega t)$ is applied along the z-axis, as follows:

$$r_L = r\begin{pmatrix} 0 \\ \sqrt{1-\sin^2\alpha\cos^2(\omega t)} \\ \sin\alpha\cos(\omega t) \end{pmatrix} \quad (1)$$

$$r_C = r\begin{pmatrix} \sin\alpha\sin(\omega t) \\ \cos\alpha \\ \sin\alpha\cos(\omega t) \end{pmatrix} \quad (2)$$

In addition, the phase delay was neglected for simplicity. Then, assuming that the sum of the other motions creates a periodic rotation in the ϕ-direction with an angular velocity of $0 \le \omega_\phi \le \omega$, rotation matrix R_ϕ can be applied as follows:

$$R_\phi = \begin{pmatrix} \cos(\omega_\phi t) & -\sin(\omega_\phi t) & 0 \\ \sin(\omega_\phi t) & \cos(\omega_\phi t) & 0 \\ 0 & 0 & 1 \end{pmatrix} \quad (3)$$

This approach enables us to easily estimate the range of rotational distances of Brownian motion in a ferrofluid, as well as the frictional heat generated. Consequently, the final expected position of the radius vector through the superposed motion of unit motion and ϕ-rotation is $\boldsymbol{r}(t) = R_\phi \boldsymbol{r}$. Therefore, the final equation of the radius vector with circular unit motion is

$$r_{C\omega_\phi}(t) = R_\phi r_C = r\begin{pmatrix} \cos\alpha\cos(\omega_\phi t)\sin(\omega t) - \cos\alpha\sin(\omega_\phi t) \\ \sin\alpha\sin(\omega_\phi t)\sin(\omega t) + \cos\alpha\cos(\omega_\phi t) \\ \sin\alpha\cos(\omega t) \end{pmatrix} \quad (4)$$

Using this equation, we can obtain their traces using mathematical expressions; that is, the range of frictional heat during the Brownian trace can be calculated. Therefore, the frictional heat of the two extreme cases ($C\omega_0$ and $C\omega_\phi$) was calculated to set the range.

$$r_{C\omega_0}(t) = r\begin{pmatrix} \sin\alpha\sin(\omega t) \\ \cos\alpha \\ \sin\alpha\cos(\omega t) \end{pmatrix} \quad (5)$$

$$r_{C\omega_\phi}(t) = r\begin{pmatrix} \sin\alpha\cos(\omega t)\sin(\omega t) - \cos\alpha\sin(\omega t) \\ \sin\alpha\sin^2(\omega t) + \cos\alpha\cos(\omega t) \\ \sin\alpha\cos(\omega t) \end{pmatrix} \quad (6)$$

At the easiest point, in the case of circular unit motion (C) and minimum ϕ-rotation ($\omega_\phi = 0$), the trace is a circle denoted by $C\omega_0$:

$$\langle Q_{C\omega_0}\rangle = 12\pi\eta V_h \omega \sin^2\alpha \quad (7)$$

To determine the maximum limit of Brownian dissipation, the parameter can be set to the circular unit motion(C) and maximum ϕ –rotation ($\omega_\phi = \omega$), denoted by $C\omega_\phi$:

$$\langle Q_{C\omega_\phi}\rangle = 6\pi\eta V_h \omega(\sin^2\alpha + 2) = \left(\frac{1}{2} + \frac{1}{\sin^2\alpha}\right)\bullet\langle Q_{C\omega_0}\rangle \quad (8)$$

calculated using Eq. (13). In conclusion, the frictional heat dissipated by a single magnetic particle per cycle can be expressed simply by multiplying the heat by the minimum trace using the proportional coefficient k_r.

$$\langle Q\rangle = k_r \bullet \langle Q_{C\omega_0}\rangle \left(1 \le k_r \le \frac{1}{2} + \frac{1}{\sin^2\alpha}\right) \quad (9)$$

Then, total volumetric dissipated Brownian heat from the ferrofluid can be calculated as

$$P_B\left[\mathrm{W/m^3}\right] = \frac{Nf\langle Q\rangle}{V_{FF}} = 6n\eta k_r V_h \omega^2 \sin^2\alpha = 6n\eta k_r V_h \left(\omega\frac{\chi'_B H_0}{M_s}\right)^2 \quad (10)$$

same as Eq. 15.

Received: 4 September 2024 Revised: 12 December 2024 Accepted: 13 January 2025
Published online: 21 March 2025

References

1. Chen, R., Romero, G., Christiansen, M. G., Mohr, A. & Anikeeva, P. Wireless magnetothermal deep brain stimulation. *Science* **347**, 1477–1480, https://doi.org/10.1126/science.1261821 (2015).
2. Sung, K. et al. Computational analysis of multichannel magnetothermal neural stimulation using magnetic resonator array. *Biomed. Eng. Lett.* **13**, 209–219, https://doi.org/10.1007/s13534-023-00267-x (2023).
3. Hescham, S.-A. et al. Magnetothermal nanoparticle technology alleviates Parkinsonian-like symptoms in mice. *Nat. Commun.* **12**, 5569, https://doi.org/10.1038/s41467-021-25837-4 (2021).
4. Zhang, Z., You, Y., Ge, M., Lin, H. & Shi, J. Functional nanoparticle-enabled non-genetic neuromodulation. *J. Nanobiotechnology* **21**, 319, https://doi.org/10.1186/s12951-023-02084-x (2023).
5. Shin, W. et al. Magnetogenetics with Piezo1 mechanosensitive ion channel for CRISPR gene editing. *Nano Lett* **22**, 7415–7422, https://doi.org/10.1021/acs.nanolett.2c02314 (2022).
6. Lee, J. U. et al. Non-contact long-range magnetic stimulation of mechanosensitive ion channels in freely moving animals. *Nat. Mater.* **20**, 1029–1036, https://doi.org/10.1038/s41563-020-00896-y (2021).
7. Young, J. H., Wang, M.-T. & Brezovich, I. A. Frequency/depth-penetration considerations in hyperthermia by magnetically induced currents. *Electron. Lett.* **16**, 358–359, https://doi.org/10.1049/el:19800255 (1980).
8. Song, G. et al. Carbon-coated FeCo nanoparticles as sensitive magnetic-particle-imaging tracers with photothermal and magnetothermal properties. *Nat. Biomed. Eng.* **4**, 325–334, https://doi.org/10.1038/s41551-019-0506-0 (2020).
9. Paysen, H. et al. Cellular uptake of magnetic nanoparticles imaged and quantified by magnetic particle imaging. *Sci. Rep.* **10**, 1922, https://doi.org/10.1038/s41598-020-58853-3 (2020).
10. Buzug, T. M.world scientific (firm). *Magnetic Nanoparticles: Particle Science, Imaging Technology, and Clinical Applications*. Proceedings of the First International Workshop on Magnetic Particle Imaging. (2010) (*Inst. of Medical Engineering, Univ. of Lubeck, Germany*, 2010).
11. Hemery, G. et al. Monocore: Vs. multicore magnetic iron oxide nanoparticles: Uptake by glioblastoma cells and efficiency for magnetic hyperthermia. *Mol. Syst. Des. Eng.* **2**, 629–639, https://doi.org/10.1039/C7ME00061H (2017).
12. Sharifianjazi, F. et al. Polymer incorporated magnetic nanoparticles: Applications for magnetoresponsive targeted drug delivery. *Mater. Sci. Eng. B* **272**, 115358, https://doi.org/10.1016/j.mseb.2021.115358 (2021).
13. Li, Z. et al. Construction of pH-responsive nanoplatform from stable magnetic nanoparticles for targeted drug delivery and intracellular imaging. *Sens. Actuators B* **375**, 132869, https://doi.org/10.1016/j.snb.2022.132869 (2023).
14. Li, J. et al. Functional material-mediated wireless physical stimulation for neuro-modulation and regeneration. *J. Mater. Chem. B* **11**, 9056–9083, https://doi.org/10.1039/d3tb01354e (2023).
15. Sebesta, C. et al. Subsecond multichannel magnetic control of select neural circuits in freely moving flies. *Nat. Mater.* **21**, 951–958, https://doi.org/10.1038/s41563-022-01281-7 (2022).
16. Tabatabaei, S. N., Girouard, H., Carret, A. S. & Martel, S. Remote control of the permeability of the blood-brain barrier by magnetic heating of nanoparticles: A proof of concept for brain drug delivery. *J. Control. Rel.* **206**, 49–57, https://doi.org/10.1016/j.jconrel.2015.02.027 (2015).
17. Chen, J., Yuan, M., Madison, C. A., Eitan, S. & Wang, Y. Blood-brain barrier crossing using magnetic stimulated nanoparticles. *J. Control. Rel.* **345**, 557–571, https://doi.org/10.1016/j.jconrel.2022.03.007 (2022).
18. Wang, Y. et al. Fe_3O_4@polydopamine nanoparticle-loaded human umbilical cord mesenchymal stem cells improve the cognitive function in Alzheimer's disease mice by promoting hippocampal neurogenesis. *Nanomed. Nanotechnol. Biol. Med.* **40**, 102507, https://doi.org/10.1016/j.nano.2021.102507 (2022).
19. Le, T. A., Bui, M. P. & Yoon, J. Theoretical analysis for wireless magnetothermal deep brain stimulation using commercial nanoparticles. *Int. J. Mol. Sci.* **20**, 2873, https://doi.org/10.3390/ijms20122873 (2019).
20. Zhang, M. et al. TRP (transient receptor potential) ion channel family: Structures, biological functions and therapeutic interventions for diseases. *Signal Transduct. Target. Ther.* **8**, 261, https://doi.org/10.1038/s41392-023-01464-x (2023).
21. Güler, A. D. et al. Heat-evoked activation of the ion channel, TRPV4. *J. Neurosci.* **22**, 6408–6414, https://doi.org/10.1523/JNEUROSCI.22-15-06408.2002 (2002).
22. Rosenfeld, D. et al. Magnetothermal modulation of calcium-dependent nerve growth. *Adv. Funct. Mater.* **32**, 2204558, https://doi.org/10.1002/adfm.202204558 (2022).
23. Askri, D. et al. Sub-acute intravenous exposure to Fe_2O_3 nanoparticles does not alter cognitive performances and catecholamine levels, but slightly disrupts plasma iron level and brain iron content in rats. *J. Trace Elem. Med. Biol.* **50**, 73–79, https://doi.org/10.1016/j.jtemb.2018.06.006 (2018).
24. Carrey, J., Mehdaoui, B. & Respaud, M. Simple models for dynamic hysteresis loop calculations of magnetic single-domain nanoparticles: Application to magnetic hyperthermia optimization. *J. Appl. Phys.* **109**, 083921, https://doi.org/10.1063/1.3551582 (2011).
25. Peter, W. J. Debye. *Polar Mol.* (1921).
26. Shliomis, M. I. & Stepanov, V. I. Theory of the dynamic susceptibility of magnetic fluids. *Adv. Chem. Phys.*, 1–30, https://doi.org/10.1002/9780470141465.ch1 (1994).
27. Biase, J. N., Whitehead, E. D., Miller, F. & Hoffman, S. Unilateral unitary inflatable penile prosthesis to correct impaired tumescence and severe penile deformity resulting from traumatic rupture of 1 corpus cavernosum. *J. Urol.* **152**, 2098–2100, https://doi.org/10.1016/s0022-5347(17)32321-2 (1994).
28. Dieckhoff, J., Eberbeck, D., Schilling, M. & Ludwig, F. Magnetic-field dependence of Brownian and Néel relaxation times. *J. Appl. Phys.* **119**, 043093, https://doi.org/10.1063/1.4940724 (2016).
29. Herrero de la Parte, B. et al. Proposal of new safety limits for in vivo experiments of magnetic hyperthermia antitumor therapy. *Cancers* **14**, 1–14, https://doi.org/10.3390/cancers14133084 (2022). Pubmed:35804855.
30. Wang, C. et al. Effective heating of magnetic nanoparticle aggregates for in vivo nano-theranostic hyperthermia. *Int. J. Nanomed.* **12**, 6273–6287, https://doi.org/10.2147/IJN.S141072 (2017). Pubmed:28894366.
31. Allia, P., Barrera, G. & Tiberto, P. Hysteresis effects in magnetic nanoparticles: A simplified rate-equation approach. *J. Magn. Magn. Mater.* **496**, 165927, https://doi.org/10.1016/j.jmmm.2019.165927 (2020).
32. Mi, Y., Ma, C., Zheng, W., Li, Z. & Zhang, M. Magnetic losses in single-domain magnetic particles. *Eur. Phys. J. Spec. Top.* **232**, 1353–1368, https://doi.org/10.1140/epjs/s11734-022-00763-8 (2023).
33. Siqueira, E. C. et al. A microscopic approach to heating rate of ferrofluid droplets by a magnetic field. *J. Appl. Phys.* **125**, 045104, https://doi.org/10.1063/1.5078648 (2019).
34. Fabris, F. et al. Adjusting the Néel relaxation time of Fe_3O_4/ZnxCo1-xFe_2O_4-core/shell nanoparticles for optimal heat generation in magnetic hyperthermia. *Nanotechnology* **32**, 065703 (2020).
35. Bui, T. Q. et al. I. Advanced characterization of magnetization dynamics in iron oxide magnetic nanoparticle tracers. *Appl. Phys. Lett.* **120**, 9–11, https://doi.org/10.1063/5.0077016 (2022).
36. Balaji, G., Narayanan, R. A., Weber, A., Mohammad, F. & Kumar, C. S. S. R. Giant magnetostriction in magnetite nanoparticles. *Mater. Sci. Eng. B* **177**, 14–18, https://doi.org/10.1016/j.mseb.2011.09.023 (2012).
37. Yoshida, T. & Enpuku, K. Simulation and quantitative clarification of AC susceptibility of magnetic fluid in nonlinear Brownian relaxation region. *Jpn. J. Appl. Phys.* **48**, 127002, https://doi.org/10.1143/JJAP.48.127002 (2009).
38. Chalifour, A. R., Davidson, J. C., Anderson, N. R., Crawford, T. M. & Livesey, K. L. Magnetic relaxation time for an ensemble of nanoparticles with randomly aligned easy axes: A simple expression. *Phys. Rev. B* **104**, 1–11, https://doi.org/10.1103/PhysRevB.104.094433 (2021).
39. Muscas, G. et al. The interplay between single particle anisotropy and interparticle interactions in ensembles of magnetic nanoparticles. *Phys. Chem. Chem. Phys.* **20**, 28634–28643 (2018).
40. Ring, H. L., Sharma, A., Ivkov, R. & Bischof, J. C. The impact of data selection and fitting on SAR estimation for magnetic nanoparticle heating. *Int. J. Hyperthermia* **37**, 100–107, https://doi.org/10.1080/02656736.2020.1810332 (2020).
41. Hoo, C. M., Starostin, N., West, P. & Mecartney, M. L. A comparison of atomic force microscopy (AFM) and dynamic light scattering (DLS) methods to characterize nanoparticle size distributions. *J. Nanoparticle Res.* **10**, 89–96, https://doi.org/10.1007/s11051-008-9435-7 (2008).
42. Anwar, M. et al. Aqueous phase transfer of oleic acid coated iron oxide nanoparticles: Influence of solvents and surfactants on stability and pharmaceutical applications of ferrofluid. *Magnetohydrodynamics* **49**, 339–343 (2013).
43. Cruz-Acuña, M., Maldonado-Camargo, L., Dobson, J. & Rinaldi, C. From oleic acid-capped iron oxide nanoparticles to polyethyleneimine-coated single-particle magnetofectins. *J. Nanoparticle Res.* **18**, 268, https://doi.org/10.1007/s11051-016-3577-9 (2016).

44. Trisnanto, S. B. & Kitamoto, Y. Field-dependent Brownian relaxation dynamics of a superparamagnetic clustered-particle suspension. *Phys. Rev. E Stat. Nonlinear Soft Matter Phys.* **90**, 1–7 (2014).
45. Yin, X., Goudriaan, J., Lantinga, E. A., Vos, J. & Spiertz, H. J. A flexible sigmoid function of determinate growth. *Ann. Bot.* **91**, 361–371, https://doi.org/10.1093/aob/mcg029 (2003).
46. Swillens, S., Dessars, B. & Housni, H. E. Revisiting the sigmoidal curve fitting applied to quantitative real-time PCR data. *Anal. Biochem.* **373**, 370–376, https://doi.org/10.1016/j.ab.2007.10.019 (2008).
47. Dennis, C. L. & Ivkov, R. Physics of heat generation using magnetic nanoparticles for hyperthermia. *Int. J. Hyperthermia* **29**, 715–729, https://doi.org/10.3109/02656736.2013.836758 (2013).
48. Gavilán, H. et al. How size, shape and assembly of magnetic nanoparticles give rise to different hyperthermia scenarios. *Nanoscale* **13**, 15631–15646, https://doi.org/10.1039/d1nr03484g (2021).
49. Liu, N. N. et al. The "field or frequency" dilemma in magnetic hyperthermia: The case of Zn–Mn ferrite nanoparticles. *J. Magn. Magn. Mater.* **555**, 169379, https://doi.org/10.1016/j.jmmm.2022.169379 (2022).
50. Liu, N. N. et al. Optimization of Zn-Mn ferrite nanoparticles for low-frequency hyperthermia: Exploiting the potential of superquadratic field dependence of magnetothermal response. *Appl. Phys. Lett.* **120**, 102403, https://doi.org/10.1063/5.0082857 (2022).
51. Yamamoto, Y. et al. Size dependence study on magnetic heating properties of superparamagnetic iron oxide nanoparticles suspension. *J. Appl. Phys.* **116**, 123906, https://doi.org/10.1063/1.4896369 (2014).
52. Mohapatra, J. et al. Size-dependent magnetic and inductive heating properties of Fe_3O_4 nanoparticles: Scaling laws across the superparamagnetic size. *Phys. Chem. Chem. Phys.* **20**, 12879–12887, https://doi.org/10.1039/c7cp08631h (2018).
53. De La Presa, P. et al. Study of heating efficiency as a function of concentration, size, and applied field in γ-Fe_2O_3 nanoparticles. *J. Phys. Chem. C* **116**, 25602–25610, https://doi.org/10.1021/jp310771p (2012).
54. Wang, B. et al. Multichannel power electronics and magnetic nanoparticles for selective thermal magnetogenetics. *J. Neural Eng.* **19**, 26015, https://doi.org/10.1088/1741-2552/ac5b94 (2022).
55. Zhang, Z., You, Y., Ge, M., Lin, H. & Shi, J. Functional nanoparticle-enabled non-genetic neuromodulation. *J Nanobiotechnology* **21**, 319, https://doi.org/10.1186/s12951-023-02084-x (2023).
56. López Espejo, M. & David, S. V. A sparse code for natural sound context in auditory cortex. *Curr. Res. Neurobiol.* **6**, 100118 (2024).
57. Zhao, K. & Ren, M. An Entorhinal-Hippocampal loop model based on non-negative sparse coding. *J. Inst. Eng. Ser. B.* https://doi.org/10.1007/s40031-024-01082-3. (2024).
58. Xu, Z., Shen, C., Hou, Y., Gao, H. & Sun, S. Oleylamine as both reducing agent and stabilizer in a facile synthesis of magnetite nanoparticles. *Chem. Mater.* **21**, 1778–1780, https://doi.org/10.1021/cm802978z (2009).
59. Hou, Y., Xu, Z. & Sun, S. Controlled synthesis and chemical conversions of FeO nanoparticles. *Angew. Chem. Int Ed Engl* **46**, 6329–6332, https://doi.org/10.1002/anie.200701694 (2007).
60. Brown, K. R. & Natan, M. J. Colloidal gold: Principles, methods, and applications. *J. Chem. Soc. Chem. Commun.* **14** (1996).
61. Cara, C. et al. Dialkylamide as both capping agent and surfactant in a direct solvothermal synthesis of magnetite and titania nanoparticles. *Cryst. Growth Des.* **15**, 2364–2372, https://doi.org/10.1021/acs.cgd.5b00160 (2015).
62. Sharifi Dehsari, H. S. et al. Effect of precursor concentration on size evolution of iron oxide nanoparticles. *CrystEngComm* **19**, 6694–6702, https://doi.org/10.1039/C7CE01406F (2017).
63. Mourdikoudis, S. et al. Oleic acid/oleylamine ligand pair: A versatile combination in the synthesis of colloidal nanoparticles. *Nanoscale Horiz* **7**, 941–1015, https://doi.org/10.1039/d2nh00111j (2022).
64. Sun, S. & Zeng, H. Size-controlled synthesis of magnetite nanoparticles. *J. Am. Chem. Soc.* **124**, 8204–8205, https://doi.org/10.1021/ja026501x (2002).
65. Yan, Z., FitzGerald, S., Crawford, T. M. & Mefford, O. T. Manganese and cobalt substituted ferrite nanoparticles synthesized via a seed-mediated drip method. *J. Phys Mater.* **4**, 034013, https://doi.org/10.1088/2515-7639/abfcd5 (2021).
66. Ealias, A. M. & Saravanakumar, M. P. A review on the classification, characterisation, synthesis of nanoparticles and their application. In *IOP Conference Series. Mater. Sci. Eng.* **263**, 032019 (2017).
67. Roy, I. Therapeutic applications of magnetic nanoparticles: Recent advances. *Mater. Adv.* **3**, 7425–7444 (2022).
68. Maazouzi, A. E. L., Masrour, R. & Jabar, A. Magnetic properties of inverse spinel: (Fe_{3+}) A (Fe_{3+} Fe_{2+}) BO4 2− Magnetite. **2**, 3871–3874 (2020).
69. Skoropata, E. et al. Magnetism of iron oxide based core-shell nanoparticles from interface mixing with enhanced spin-orbit coupling. *Phys. Rev. B* **89**, 1–9, https://doi.org/10.1103/PhysRevB.89.024410 (2014).
70. Raikher, Y. L. & Stepanov, V. I. Physical aspects of magnetic hyperthermia: Low-frequency AC field absorption in a magnetic colloid. *J. Magn. Magn. Mater.* **368**, 421–427, https://doi.org/10.1016/j.jmmm.2014.01.070 (2014).